International Journal of General Medicine

Dovepress
Taylor & Francis Group

Open Access Full Text Article

ORIGINAL RESEARCH

Exploring the Mechanisms of the Traditional Herbal Formula Sanshen Dan Against Myocardial Ischemia-Reperfusion Injury: An Integrated Strategy Combining Serum Pharmacochemistry, Network Pharmacology, and Molecular Docking

Yidi Ma[1,*], Xue Fang[1,*], Yin Fu[1], Weitai Kong[1], Qiang Fu[1], Rui Qie[2]

[1]School of Basic Medical Sciences, Heilongjiang University of Traditional Chinese Medicine, Harbin, Heilongjiang, People's Republic of China; [2]The First Affiliated Hospital, Heilongjiang University of Traditional Chinese Medicine, Harbin, Heilongjiang, People's Republic of China

*These authors contributed equally to this work

Correspondence: Qiang Fu; Rui Qie, Heilongjiang University of Traditional Chinese Medicine, Harbin, Heilongjiang, People's Republic of China, Tel +15124527001; +13804523921, Email fuqiang@hljucm.edu.cn; 13804523921@163.com

International Journal of General Medicine downloaded from https://www.dovepress.com/
For personal use only.

Objective: Myocardial ischemia-reperfusion injury (MIRI) is a critical clinical challenge in cardiovascular disease management. Sanshen Dan (SSD), a clinically validated traditional Chinese medicine formula, exerts therapeutic effects on MIRI, but its chemical composition and underlying mechanism remain unclear. This study aimed to systematically elucidate the cardioprotective mechanism of SSD against MIRI using an integrated strategy.

Methods: An integrated approach combining serum pharmacochemistry, network pharmacology, machine learning, molecular docking, and molecular dynamics simulation was adopted. 1. Ultra-high performance liquid chromatography-tandem mass spectrometry (UHPLC-MS/MS) was used to identify blood-absorbed components of SSD after oral administration to Sprague-Dawley rats. 2. Potential targets of these components were predicted via public databases, and overlapping targets with MIRI-related genes were screened to construct a compound-target network, followed by Gene Ontology (GO) and Kyoto Encyclopedia of Genes and Genomes (KEGG) enrichment analyses. 3. Three machine learning algorithms (random forest, SVM-RFE, LASSO regression) were applied to identify core therapeutic targets. 4. Molecular docking and 100 ns molecular dynamics simulations were performed to verify the binding affinity and stability of ligand-receptor complexes.

Results: A total of 44 blood-absorbed active components of SSD were identified, including flavonoids, saponins, lignans, and phenolic acids. A total of 392 potential therapeutic targets were screened out, which were mainly enriched in apoptosis, HIF-1, TNF-α, and cAMP signaling pathways. Machine learning analysis identified Mmp14, Htr2b, and Ctnnb1 as core targets, and the constructed nomogram model showed excellent predictive performance (AUC = 1, C-index = 1). Molecular docking indicated that 6 core components (eg, Kaempferide-4′-methyl ether-3-glucoside, Licurazide) exhibited strong binding affinity to the core targets, and molecular dynamics simulations confirmed the high stability of these complexes, with mean binding free energy ranging from −20.58 kcal/mol to −34.31 kcal/mol.

Conclusion: SSD exerts cardioprotective effects against MIRI via a "multi-component, multi-target, multi-pathway" mode. Its core blood-absorbed components may alleviate MIRI by regulating core targets including Mmp14 and Ctnnb1, and modulating key signaling pathways such as TNF-α and HIF-1. This study provides a scientific basis for the clinical application of SSD and further exploration of traditional Chinese medicine compound formulas.

Keywords: myocardial ischemia-reperfusion injury, network pharmacology, molecular docking, multi-target mechanism, pharmacological basis

https://doi.org/10.2147/IJGM.S577525
Received: 29 October 2025
Accepted: 28 January 2026
Published: 6 February 2026

© 2026 Ma et al. This work is published and licensed by Dove Medical Press Limited. The full terms of this license are available at https://www.dovepress.com/terms.php and incorporate the Creative Commons Attribution – Non Commercial (unported, v4.0) License (http://creativecommons.org/licenses/by-nc/4.0/). By accessing the work you hereby accept the Terms. Non-commercial uses of the work are permitted without any further permission from Dove Medical Press Limited, provided the work is properly attributed. For permission for commercial use of this work, please see paragraphs 4.2 and 5 of our Terms (https://www.dovepress.com/terms.php).

Introduction

Ischemic Heart Disease (IHD) remains one of the leading global causes of cardiovascular mortality. In developed countries, the implementation of tobacco control policies, standardized use of statins, and optimized hypertension management systems have significantly reduced IHD-related deaths. However, in developing countries, factors such as delayed translation of evidence-based medical advances and the rising prevalence of metabolic syndromes (eg, obesity and diabetes) contribute to persistently high rates of IHD incidence and mortality. Myocardial ischemia/reperfusion injury (MIRI) constitutes the pathophysiological basis of IHD.[1] MIRI refers to a series of complex pathophysiological responses triggered upon the restoration of blood flow (reperfusion) following ischemic episodes, which exacerbate pre-existing tissue damage, impair cardiac function, lead to irreversible cardiomyocyte injury, and expand the infarct zone. Although current clinical strategies—such as percutaneous coronary intervention, coronary artery bypass grafting, and thrombolytic therapy—aim to restore perfusion and oxygen supply to ischemic myocardium and facilitate ventricular remodeling,[2] these treatments may paradoxically aggravate myocardial damage through mechanisms such as mitochondrial permeability transition and other pathological cascades.[3] This underscores the critical need to advance research into the mechanisms of traditional Chinese medicine in treating MIRI.

According to TCM theory integrated with modern clinical practice, myocardial ischemia-reperfusion injury is classified under the pattern of Xiong Bi and heart pain, characterized chiefly by symptoms aligning with the axiom that "prolonged Xiong Bi manifests as blood stasis and qi deficiency". Professor Duan Fujin posits that Xiong Bi arises from root deficiency and branch excess, where the root deficiency primarily involves qi deficiency, and branch excess correlates with blood stasis. Supported by evidence-based clinical studies, he established "tonifying qi and activating blood circulation" (Yi Qi Huo Xue) as the core therapeutic strategy for this disease. Guided by the holistic concept and treatment based on syndrome differentiation, and further refined through clinical experience and observation, TCM has been shown to not only ameliorate clinical symptoms of myocardial ischemia-reperfusion injury, delay its progression, and prevent complications, but also mitigate certain adverse effects associated with Western pharmaceutical interventions.

The traditional Chinese medicine compound prescription SanShenDan Decoction (SSD) was formulated by Professor Duan Fujin, a National Master of Chinese Medicine, based on his summation of the medicinal experiences of physicians across generations. SSD comprises the following herbal ingredients: White Ginseng (Panax ginseng C.A. Mey. abbreviation: BS) 15 g; Notoginseng (Panax notoginseng (Burk.) F.H. Chen abbreviation: SQ) 3 g; Chuanxiong Rhizome (Ligusticum chuanxiong Hort. abbreviation: CX) 15 g; Chinese Angelica (Angelica sinensis (Oliv.) Diels abbreviation: DG) 15 g; Dragon's Blood (Dracaena cochinchinensis (Lour.) S.C. Chen abbreviation: XJ) 3 g; Danshen Root (Salvia miltiorrhiza Bunge abbreviation: DS) 20 g; Astragalus Root (Astragalus membranaceus (Fisch.) Bunge abbreviation: HQ) 30 g; Schisandra Berry (Schisandra chinensis (Turcz.) Baill. abbreviation: WWZ) 15 g; Honey-fried Licorice (Glycyrrhiza uralensis Fisch. ex DC. abbreviation: ZGC) 15 g. This formula is made up of 9 traditional Chinese Medicine. According to the compatibility rules of traditional Chinese medicine prescriptions, the medicinal materials in SSD can be divided into different components. BS is the Sovereign drug, tonifying and replenishing qi; HQ and SQ are the Minister drugs, with HQ enhancing the efficacy of the Sovereign drug and tonifying the qi of the entire body (both exterior and interior), while SQ resolves stasis, stops bleeding, and promotes blood circulation to alleviate pain. DS, DG, CX, and XJ are the Assistant herbs: DS activates blood, relieves pain, and resolves stasis; DG tonifies blood while promoting blood circulation, and both DS and DG conduct the herbs' entry to the heart meridian; CX promotes blood circulation and regulates the flow of qi, replenishing blood without causing stagnation; XJ removes blood stasis and alleviates pain. When all these herbs are combined, they can achieve the effects of replenishing qi, activating blood, resolving stasis, and relieving pain. In modern medicine, it is frequently applied for the treatment of ischemic heart diseases, including coronary heart disease, myocardial ischemia-reperfusion injury, myocardial infarction, and the like. Based on clinical observations, SSD benefits MIRI patients by improving symptoms such as chest tightness and stabbing pain, shortness of breath and fatigue, aversion to cold and cold limbs, purple and dark lips, and ECG manifestations. In this study, we used Ultrahigh performance liquid chromatography-mass spectrometry (UHPLC-MS/MS) to identify and quantify the compounds in SSD, analyzed the blood-entry components of SSD to screen key compounds for predicting

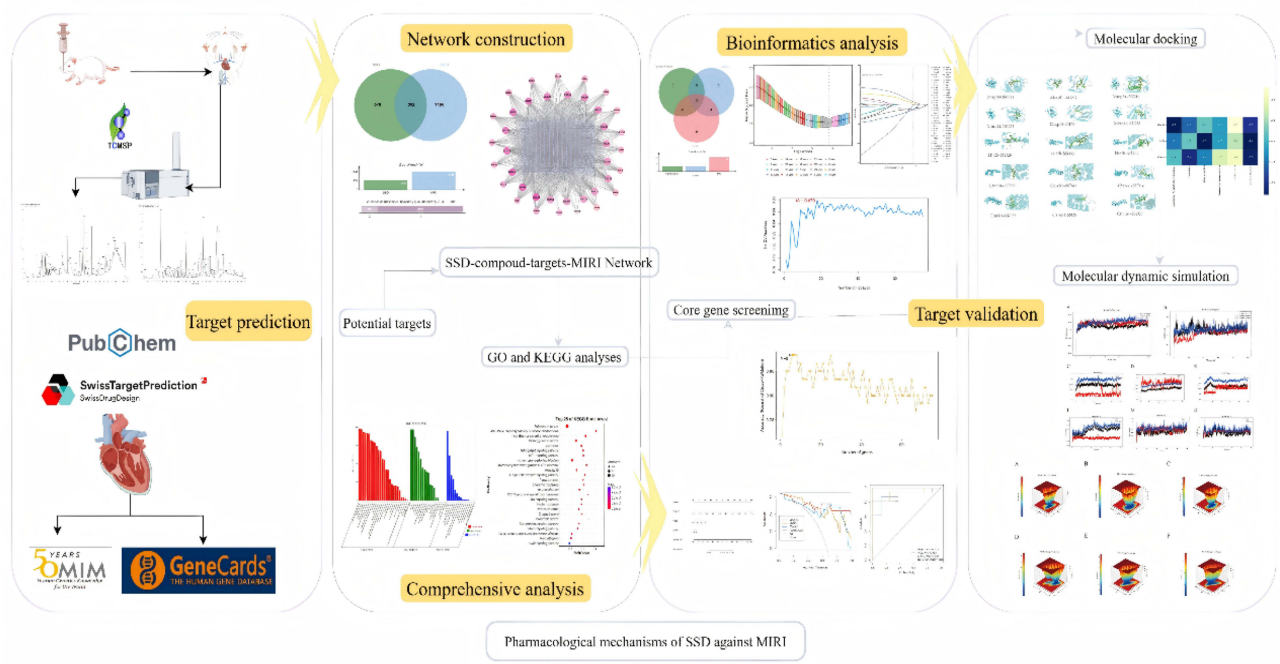

Figure 1 A flow-chart of this study.

key targets, applied authoritative databases (with high prediction accuracy) and literature combined with disease databases to screen potential disease targets, and constructed a "drug entry components - core efficacy targets - important pathways of action" network using network pharmacology and functional enrichment. Subsequently, we built a "drug entry components - core efficacy targets - important pathways" network to analyze the potential pharmacodynamic mechanism of SSD. Based on these results, we employed machine learning to detect ligand-target interactions with key efficacy targets and related protein expression from previous results, and further validated the corresponding targets and their effects on treating MIRI with SSD. Finally, we used machine learning to detect ligand-target interactions and related protein expression from prior results to validate SSD's targets and pathways in treating MIRI, laying the foundation for further mechanistic elucidation (Figure 1).

Materials and Methods

Screening the Active Ingredients and Targets of SSD

Preparation of SSD

SSD was composed of 9 natural medicinal components, including 15 g white ginseng, 3 g Panax notoginseng, 15 g Ligusticum chuanxiong, 15 g Angelica sinensis, 3 g Dragon's blood, 20 g Salvia miltiorrhiza, 30 g Astragalus membranaceus, 15 g Schisandra chinensis, and 15 g honey-fried Glycyrrhiza uralensis, provided by the Traditional Chinese Medicine Pharmacy of the First Affiliated Hospital of Heilongjiang University of Chinese Medicine. All the medicinal herbs were added to water, which was 10 times the total amount of the herbs, soaked for 30 minutes, and then decocted twice, with each decoction lasting for 1 hour. After the above medicinal slices were decocted twice according to the standard method, the filtrates were combined. Then, the administration dose for rats was calculated based on the human-animal body surface area conversion method. Subsequently, the mixture was concentrated in a water bath at 80 °C to a crude drug concentration of 3.54 $g \cdot mL^{-1}$, stored in a refrigerator at 4 °C, and warmed up to 37 °C before being used for gavage.

Animals

All animal pro-cedures conformed to the Guide for the Care and Use of Laboratory Animals published by the US National Institutes of Health and were approved by the Animal Ethical Committee of Heilongjiang University of Chinese

Medicine. (NO. 2024102503). Twelve male Sprague-Dawley (SD) rats of SPF grade, with a body weight of 200 ± 10 g, were provided by the Center for Drug Safety Evaluation (GLP Laboratory) of Heilongjiang University of Chinese Medicine (Animal License No.: SCXK(Liao)2022–0001). The animals were housed in the Laboratory of Formula Analysis at Heilongjiang University of Chinese Medicine under controlled conditions: room temperature 24 ± 2 °C, relative humidity 55 ± 3%, and adequate ventilation. All animal procedures were conducted in compliance with the university's guidelines for the care and use of laboratory animals and adhered to the 3R (Replacement, Reduction, Refinement) principles. The rats were provided with a standard laboratory diet and had free access to food and water for at least one week before the experiment.

Sample Preparation

After one week of acclimatization, the rats were randomly assigned to a control group and a SSD-treated group, with six rats in each group. All animals had free access to food and water. The SSD-treated groups received SSD via oral gavage, while the control group was administered an equal volume of distilled water. The administration was performed once daily for seven consecutive days. Sixty minutes after the last administration, the rats were anesthetized by intraperitoneal injection of 2% pentobarbital sodium (2 mg/kg). Blood samples were collected from the abdominal aorta and allowed to stand at room temperature for one hour. Subsequently, the samples were centrifuged at 4°C and 4000 r/min for 20 minutes. The supernatant was collected and stored at –80°C for further analysis.

Identification of Major Chemical Components of SSD by Ultrahigh Performance Liquid Chromatography-Mass Spectrometry (UHPLC-MS/MS)

The chemical constituents of SSD and its bioactive components absorbed into the bloodstream were characterized using ultra-high-performance liquid chromatography coupled with tandem mass spectrometry (UHPLC–MS/MS). For the SSD sample, 200 mg was accurately weighed into a 15 mL centrifuge tube, followed by the addition of 10 mL of 50% methanol (v/v). The mixture was vortexed thoroughly, and 1 mL of the supernatant was centrifuged at 14,000 rpm for 5 min. The resulting supernatant was filtered through a 0.22 μm membrane and transferred to an autosampler vial for UHPLC–MS/MS analysis. A blank sample was prepared following the same protocol. For plasma samples, 100 μL of plasma was mixed with 500 μL of acetonitrile in a 1.5 mL EP tube to precipitate proteins. After being vortex-mixed for 2 min and centrifuged at 14,000 rpm for 5 min, 500 μL of the supernatant was collected and evaporated to dryness under a gentle nitrogen stream. The residue was reconstituted in 100 μL of 50% acetonitrile aqueous solution and injected for analysis. A blank plasma sample was processed identically. Chromatographic separation was achieved using an ACQUITY UPLC HSS T3 column (100 mm × 2.1 mm, 1.8 μm; Waters) with a mobile phase consisting of (A) deionized water with 0.1% formic acid and (B) acetonitrile with 0.1% formic acid (LC–MS grade, Fisher Chemical). The gradient elution program was as follows: 0–15 min, 100%–80% A; 15–50 min, 80%–0% A; 50–60 min, 0% A; 60–70 min, 0%–100% A. The flow rate was 0.25 mL/min, the column temperature was maintained at 35 °C, and the injection volume was 10 μL with the autosampler temperature set at 4 °C. Mass spectrometric detection was performed on a Waters Synapt G2-Si Qtof instrument equipped with an electrospray ionization (ESI) source operating in both positive and negative ion modes with MSe acquisition. The full-scan mass range was m/z 50–1500. Leucine enkephalin (1 ppm) was used as the reference lock mass, scanned every 15s for 0.3s. The capillary voltage was set to 3.0 kV in positive mode and 2.5 kV in negative mode. The cone voltage was set to 40 V, with collision energies of 10 eV (low) and 50 eV (high). The ion source temperature was maintained at 125 °C, and the desolvation temperature was 500 °C. The cone gas flow rate was 50 L/h, while the desolvation gas flow was 800 L/h. The total run time was 70 minutes. The system was controlled using Waters UPLC I-Class coupled with Synapt G2-Si Qtof, and data acquisition was performed with UNIFI software incorporating a dedicated natural product workflow. Blank plasma samples served as the reference, while plasma collected after SSD administration was analyzed as the test group. Compound identification was conducted against a theoretical MS/MS library containing 6400 natural products for comprehensive compositional analysis.

Prediction of Putative SSD Prescription Targets

Following the identification of blood-absorbed components of SSD, their chemical structures were retrieved from the PubChem (http://pubchem.ncbi.nlm.nih.gov/) and WeiShengXin (http://www.bioinformatics.com.cn/). Potential protein

targets of these components were predicted using the SwissTargetPrediction (http://www.swisstargetprediction.ch/) and the Traditional Chinese Medicine Systems Pharmacology (TCMSP, http://lsp.nwu.edu.cn/tcmsp.php) Pubchem. The resulting target proteins were subsequently standardized and annotated using the UniProt database.

MIRI-Associated Therapeutic Targets

Target Prediction for Potential Compounds

Potential therapeutic targets of SSD against MIRI were identified through the following procedure: Disease-associated targets were retrieved from the OMIM and GeneCards (http://www.genecards.org/) using the keyword "myocardial ischemia reperfusion injury", set the search species to Homo sapiens. After removing duplicates, the resulting disease-related targets were intersected with the target proteins of SSD's bioactive components. The overlapping targets were considered as potential candidate targets through which SSD may exert its therapeutic effects on MIRI.

Construction of the Active Compound-Target Network

The blood-absorbed components of SSD and their corresponding potential therapeutic targets were compiled in an Excel spreadsheet, with each component assigned a numerical identifier. The component-target interactions were established, and the data were subsequently imported into Cytoscape (Version 3.10.0) to construct a compound-target network.

GO Enrichment and KEGG Pathway Analysis

To investigate the biological functions of the potential MIRI-related targets, Gene Ontology (GO) and Kyoto Encyclopedia of Genes and Genomes (KEGG) pathway enrichment analyses were performed using the OmicShare cloud platform (OmicShare, GeneDenovo Biotechnology). The overlapping targets identified in Construction of the Active Compound-Target Network were converted to official gene IDs and analyzed under the species background "Homo sapiens". A significance threshold of $P < 0.05$ was applied, and functional annotations of enriched terms were derived from the corresponding databases.

Machine Learning

Two gene expression datasets related to MIRI, GSE160516 and GSE83472, were obtained from the Gene Expression Omnibus (GEO) database. After batch effect removal using the "sva" package in R, a combined dataset comprising 16 MIRI samples and 8 sham-operated samples was constructed. Given the scarcity of human MIRI samples, the "homologene" package was employed to perform human-mouse homologous gene conversion for key genes involved in SSD treatment of MIRI.

To identify core therapeutic targets, three machine learning algorithms were applied: random forest, support vector machine-recursive feature elimination, and LASSO regression using their respective R packages ("randomForest", "SVM-RFE", and "glmnet"). The characteristic genes identified by these methods were intersected to pinpoint central targets.

Multivariate logistic regression was then used to evaluate the identified hub targets. The "Pro" package was applied to calculate the area under the receiver operating characteristic (ROC) curve (AUC) to assess their diagnostic value in MIRI. A nomogram was developed to predict the probability of MIRI occurrence, and decision curve analysis (DCA) was performed to evaluate the clinical utility of the model. Internal validation was carried out using bootstrap resampling with 1000 iterations, and the predictive performance was quantified using the concordance index (C-index). Discriminative ability was measured by AUC, with a value above 0.80 considered acceptable The goodness-of-fit was assessed using the Hosmer–Lem show test, and the net clinical benefit of the logistic regression model was evaluated by decision curve analysis (DCA).

Molecular Docking

The amino acid sequences of the core target proteins (Mmp14, Htr2b, Ctnnb1) were obtained from the UniProt database. The corresponding three-dimensional crystal structures were downloaded from the RCSB Protein Data Bank (PDB, https://www.rcsb.org/). The original PDB structures were imported into PyMOL software. All redundant ligands, bound

water molecules, and inorganic salt ions in the protein crystal structures were removed to avoid interference with subsequent docking simulations. The processed protein structures were imported into AutoDockTools 1.5.7. The protonation state of the protein was adjusted according to the physiological environment (pH 7.4). Polar hydrogen atoms were added to the protein, and non-polar hydrogen atoms were merged. The Kollman united-atom charge was assigned to the protein to complete the preprocessing. The 2D structures of the core components were retrieved from the PubChem database (https://pubchem.ncbi.nlm.nih.gov/), imported into Chem3D software for structural optimization and 3D structure construction, followed by the removal of water molecules and redundant ligands using PyMOL software.

Molecular docking was performed using AutoDock 1.5.7. A grid box was centered on the receptor protein and adjusted to encompass the entire predicted binding pocket. Docking simulations were carried out and evaluated using the Vina scoring algorithm. The resulting docking poses were visualized and analyzed using PyMOL.

Molecular Dynamics Simulation

Molecular dynamics (MD) simulations were conducted using Gromacs version 2022.3. Small molecules were parameterized with the GAFF force field via AmberTools22. Hydrogen atoms were added, and RESP charges were calculated using Gaussian 16W. Simulations were conducted at a constant temperature of 300 K and pressure of 1 bar. The Amber99sb-ildn force field was applied, with water molecules represented using the Tip3p model, and sodium ions were added to neutralize the system charge. Energy minimization was carried out using the steepest descent algorithm. Subsequently, the system was equilibrated under the NVT (canonical ensemble) and NPT (isothermal-isobaric ensemble) conditions, each for 100,000 steps with a coupling constant of 0.1 ps and a duration of 100 ps. Production MD was run for 10 ns (5,000,000 steps with a 2-fs time step). Trajectories were analyzed using built-in Gromacs tools to calculate the root mean square deviation (RMSD), root mean square fluctuation (RMSF), radius of gyration, and binding free energy (MM/GBSA), as well as to construct free energy landscapes.

Results

Identification and Analysis of Blood-Absorbed Components

A UHPLC-MS/MS method was established for quality control and compound identification of SSD. Base peak intensity (BPI) chromatograms were acquired in both positive (Figure 2A) and negative (Figure 2B) ion modes. Based on comparisons with reference standards and relevant databases, a total of 44 major compounds were tentatively identified in SSD. These compounds belong to various classes, including flavonoids, saponins, lignans, and phenolic acids. Detailed characterization of the absorbed SSD components into the bloodstream is provided in Table 1.

Target Prediction for SSD in the Treatment of MIRI

Analysis of Blood-Absorbed Component Targets and Disease Targets

Through UHPLC-MS/MS analysis, 216 chemical components derived from Chinese materia medica present in SSD were collected from the mass spectrometry database, while 46 chemical components were detected in blank plasma. Based on the above findings, compounds that were present in plasma after drug administration but absent or exhibiting abundance close to baseline noise in blank plasma were identified as potential blood-entering components, totaling 44. The total ion chromatograms in positive and negative ion modes are shown in Figure 2A and B, respectively. Detailed analysis results of the blood-entering components are presented in Table 1. After standardizing the chemical component names using the Uniprot database platform, 38 component targets were predicted and screened according to the method described in Prediction of Putative SSD Prescription Targets. Following the procedure under Target Prediction for Potential Compounds, a total of 1820 disease-related targets were retrieved and deduplicated. Using a Venn diagram tool, the intersection of these two sets was taken, yielding 392 potential therapeutic targets of SSD for the treatment of MIRI (Figure 2C).

Network Analysis

The blood-entering components and disease targets were imported into Cytoscape 3.10.0 to construct a compound-target interaction network of SSD, which comprised 430 nodes and 1820 edges (Figure 2D). Given the complexity of the

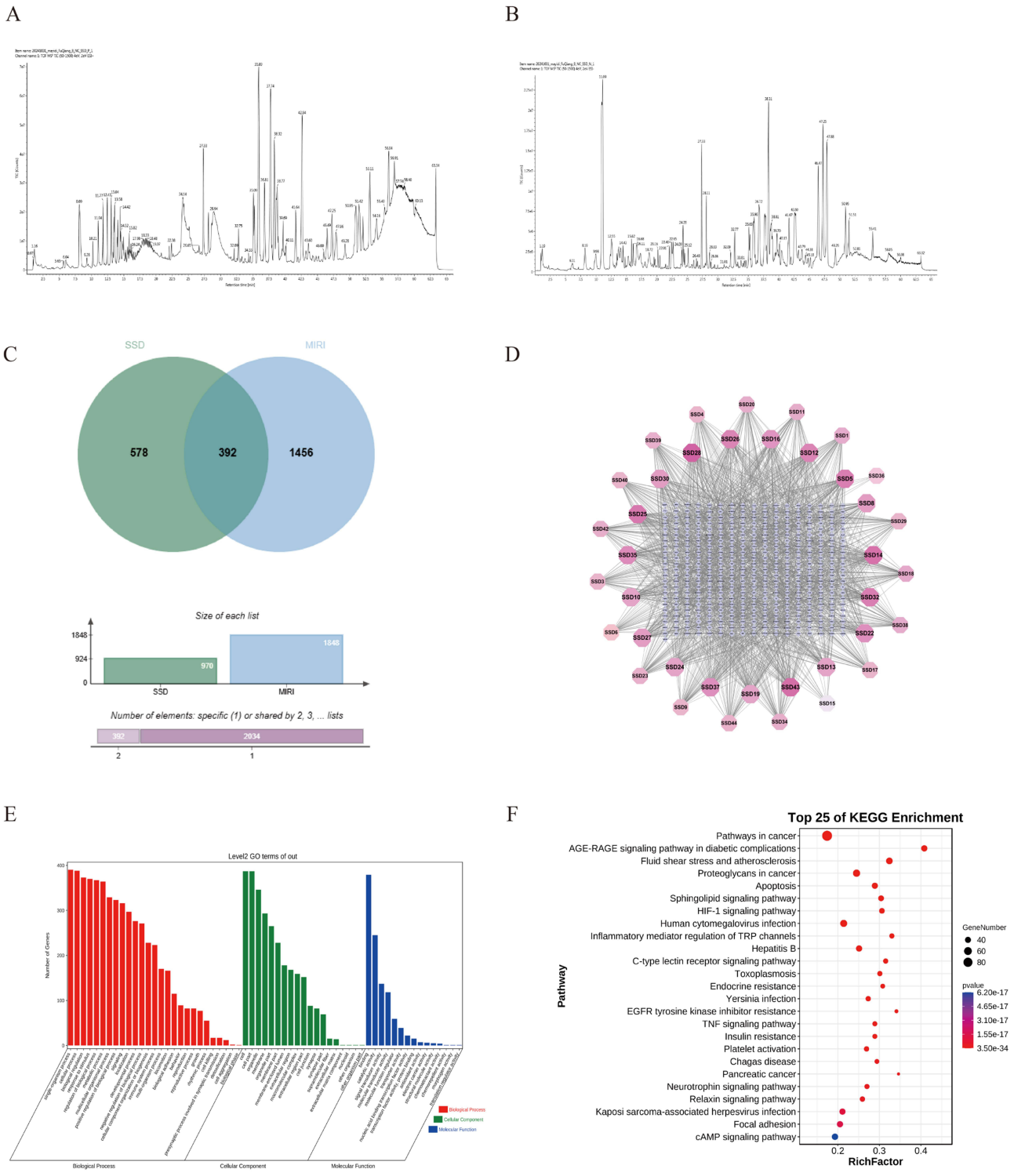

Figure 2 Construction of the Compound–Target Network and Screening of Disease Targets (**A** and **B**) UHPLC–MS/MS total ion chromatograms of the blood-absorbed components of SSD in (**A**) positive and (**B**) negative ion modes. (**C**) Venn diagram representing the overlap between targets of blood-absorbed components of SSD and myocardial ischemia–reperfusion injury (MIRI)-related targets. (**D**) Compound–target network of SSD bioactive compounds and key targets. (**E** and **F**) Functional enrichment analysis of key targets: (**E**) Gene Ontology (GO) terms and (**F**) KEGG pathways.

https://doi.org/10.2147/IJGM.S577525

Table 1 Information of Blood-Absorbed Components of SSD

No	Compound	m/z	Mass Deviation (ppm)	Retention Time (Min)	Peak Area	Compound	Molecular Formula	Molecule Structure
1	Liquiritigenin	257.0812	1.3	14.33	54927	+H	C15H12O4	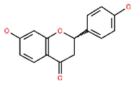
2	Ginsenoside Ro	957.4883	−17.8	18.41	54200	+H	C48H76O19	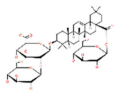
3	Methyl hexadecanoate	288.2903	2	29.49	44890	+H	C17H34O2	
4	Cnidilide	217.1186	−6.1	24.73	23190	+Na	C12H18O2	
5	Ferulic acid	193.053	12.5	13.56	10724	-H	C10H10O4	
6	Choline	104.1069	−0.4	1.09	9030	-e	C5H14NO	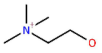
7	(6αR, 11R)-10-Hydroxy -3,9-dimethoxy-pterocarpan	301.1079	3	18.14	8581	+H	C17H16O5	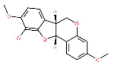
8	Sugiol	301.2171	3	43.86	5122	+H	C20H28O2	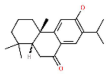
9	Hexadecanoic acid	279.233	12.5	28.64	4902	+Na	C16H32O2	
10	Linolenic acid	301.2175	12.3	46.17	4706	+Na	C18H30O2	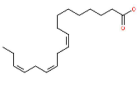

(*Continued*)

https://doi.org/10.2147/IJGM.S577525

Table 1 (Continued).

No	Compound	m/z	Mass Deviation (ppm)	Retention Time (Min)	Peak Area	Compound	Molecular Formula	Molecule Structure
11	Dracorubin	487.1625	15.1	12.78	4282	-H	C32H24O5	
12	3-Hydroxy-4-methoxy-cinnamic acid	194.0612	13.9	15.65	3471	+e	C10H10O4	
13	Isoliquiritigenin	257.0819	4.2	10.78	3316	+H	C15H12O4	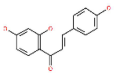
14	Ginsenoside Rf	823.4779	−4.2	19.4	2950	+Na	C42H72O14	
15	3-Hydroxymethy-2-furfural	149.0238	19.5	23.71	2802	+Na	C6H6O3	
16	Tigogenin	434.3608	−4.7	54.61	2402	+H	C27H44O3	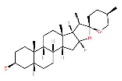
17	Neocnidilide	217.1197	−0.7	26.84	2181	+Na	C12H18O2	
18	1,2-Dihydrotanshinonel	279.1025	3.4	29.28	1982	+H	C18H14O3	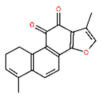
19	Formononetin	286.1064	−3.5	38.94	1970	+H	C16H12O4	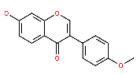

(*Continued*)

https://doi.org/10.2147/IJGM.S577525

Table 1 (Continued).

No	Compound	m/z	Mass Deviation (ppm)	Retention Time (Min)	Peak Area	Compound	Molecular Formula	Molecule Structure
20	2′-Hydroxy-7,3′,4′-trimethoxy-isoflavan	351.0987	−5.2	17	1887	+Cl	C18H20O5	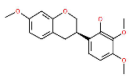
21	Pseudo-ginsenoside Rp1	764.4474	17.4	20.36	1577	-e	C41H64O13	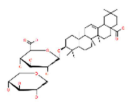
22	Licochalcone B	287.0931	5.8	17.98	1327	+H	C16H14O5	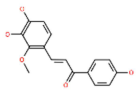
23	7,2′-Dihydroxy-3′,4′-dimethoxy-isoflavan	325.1084	11.4	23.44	1230	+Na	C17H18O5	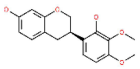
24	Gomisin C (Schisantherin A)	537.2144	4.6	34.91	1212	+H	C30H32O9	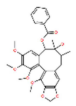
25	Gomisin B (Schisantherin B)	537.2144	9	34.91	1212	+Na	C28H34O9	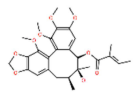
26	9,10-Dimethoxy-pterocarpan-3-O-β-D-glucoside	463.1613	3.1	19.82	1166	+H	C23H26O10	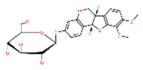
27	Wuweizi alcohol A	450.2529	9.4	26.49	1115	+H	C24H32O7	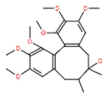
28	Kaempferide-4′-methylether -3-glucoside	463.1257	4.8	17.51	979	+H	C22H22O11	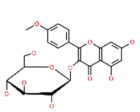

(*Continued*)

Table 1 (Continued).

No	Compound	m/z	Mass Deviation (ppm)	Retention Time (Min)	Peak Area	Compound	Molecular Formula	Molecule Structure
29	Methyl3,4-dimethoxybenzoate	219.0667	17.9	15.82	905	+Na	C10H12O4	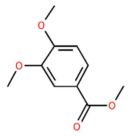
30	2,4-Dihydroxyaceto-phenone	153.0554	5.2	19.74	854	+H	C8H8O3	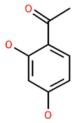
31	Xiongterpene	625.3788	−12	61.91	826	+Na	C39H54O5	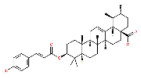
32	Danshenxinkun D	337.1491	16.9	36.45	826	+H	C21H20O4	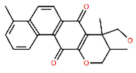
33	Astragaline C	271.1339	18.6	20.8	768	+H	C12H15NO5	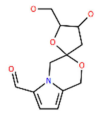
34	Spathulenol	243.1753	13.8	27.42	649	+Na	C15H24O	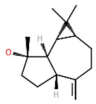
35	Schizandin C	383.1539	10	5.39	638	-H	C22H24O6	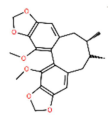
36	Alloocimene	159.1174	18.9	37.98	634	+Na	C10H16	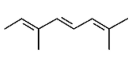

(*Continued*)

https://doi.org/10.2147/IJGM.S577525

Table 1 (Continued).

No	Compound	m/z	Mass Deviation (ppm)	Retention Time (Min)	Peak Area	Compound	Molecular Formula	Molecule Structure
37	3′-Methoxy-5′-hydroxyisoflavone -7-O-β-D-glucoside	445.1063	−17.2	16.69	593	-H	C22H22O10	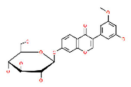
38	(-)-Gomisin L1	387.1825	6	35.44	489	+H	C22H26O6	
39	Isocryptotanshinone	297.1486	0.4	9.07	483	+H	C19H20O3	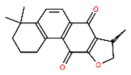
40	4-Hydroxy-3-butylphthalide	207.1028	5.8	17.82	457	+H	C12H14O3	
41	Astragaline E	292.1042	−4.1	1.4	386	-e	C14H16N2O5	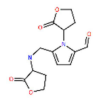
42	7-Methoxycoumarin	194.082	4.5	15.69	382	+H	C10H8O3	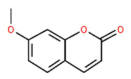
43	Licurazide	549.1688	13.6	14.61	377	-H	C26H30O13	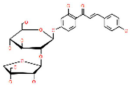
44	7,2′,3′-Trihydroxy-4′-methoxy-isoflavan	289.1076	1.9	18.91	360	+H	C16H16O5	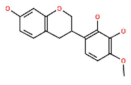

compound names, numerical identifiers were used for simplification (details provided in Table 1). In the network, the outer pink nodes represent the blood-entering components of SSD, the central purple nodes denote the target proteins, and the node color intensity is proportional to the Degree value. The edges reflect the interactions between compounds and targets.

Functional Enrichment Analysis

To investigate the potential functions of these 392 key targets, gene annotation and functional enrichment analysis were conducted using the Omicshare GeeDoo Cloud Platform. For GO functional enrichment analysis, the top 20 ranked terms were selected based on $P < 0.05$ and gene count greater than the mean value. A total of 59 GO terms were identified, including 25 biological process (BP) terms, 19 cellular component (CC) terms, and 15 molecular function (MF) terms (Figure 2E). The BP terms primarily involved in the treatment of myocardial I/R injury included: alleviating oxidative stress; inhibiting inflammatory response; regulating programmed cell death; and improving abnormal energy metabolism. The top-ranked CC terms mainly involved mitochondria, membrane, extracellular matrix, and lysosome. The MF terms were primarily associated with regulating redox homeostasis, inhibiting inflammatory factor signal transduction, interfering with programmed cell death, maintaining ion homeostasis, energy metabolism reprogramming, modulating transcription factor binding to target genes, protein kinase activity, and regulating nitric oxide synthase. To further investigate the signaling pathway mechanisms of SSD in treating MIRI, KEGG pathway analysis was conducted. Based on $P < 0.05$ and gene count greater than the mean value, the top 25 pathways were selected according to P-value and gene count, and a bubble chart was generated (Figure 2F). The analysis results mainly involved apoptosis and signaling pathways such as HIF-1, TNF-α, cAMP, and TRP.

Machine Learning

Key genes in the training dataset were screened using three distinct machine learning algorithms. Datasets GSE160516 and GSE83472 were processed using the "sva" R package to address batch effects and comprehensively integrate the data, resulting in 16 MIRI samples and 8 Sham samples. Comprehensive screening was performed using Random Forest (Figure 3B), Support Vector Machine-Recursive Feature Elimination (SVM-RFE) (Figure 3C), and Lasso regression (Figure 3D) (as outlined in Figure 3A), leading to the identification of three key genes: Mmp14, Htr2b, and Ctnnb1 (Figure 3E). Based on these genes, a logistic regression model was developed and presented as a nomogram to enhance diagnostic accuracy, optimize the disease prediction framework, and improve result reliability. The model demonstrated excellent predictive performance (AUC = 1, C-index = 1) (Figure 3F), further validating the significant impact of these key genes on MIRI progression. To ensure the accuracy of the receiver operating characteristic (ROC) curve, the bootstrap method was applied with random resampling (n = 1000 bootstraps) and replacement. Decision curve analysis confirmed the stability of the model (Figure 3G).

Molecular Docking Study

Using network pharmacology, we have identified six core active components of SSD: Kaempferide-4′-methyl ether-3-glucoside, Licurazide, Ginsenoside Rf, Gomisin B (Schisantherin B), Ferulic acid, and Danshenxinkun D. Subsequently, molecular docking was performed between these compounds and the three key genes (Mmp14, Htr2b, and Ctnnb1) obtained from machine learning. The Autodock results confirmed the affinity (also referred to as binding capability) between the identified SSD blood-entering components and the key targets. It is widely accepted that lower binding energy indicates stronger molecular affinity; typically, a binding energy below 5 kJ/mol suggests strong binding between the ligand and receptor.[4] This analysis aimed to determine the critical role of these compounds in the treatment of MIRI. Visualization was conducted using PyMOL. The results indicated that Kaempferide-4′-methyl ether-3-glucoside, Licurazide, and Ginsenoside Rf exhibit favorable binding affinity to all proteins. Specifically, the molecular docking results revealed that Kaempferide-4′-methyl ether-3-glucoside formed five binding sites with Mmp14 and four with Ctnnb1; Licurazide showed four binding sites with Ctnnb1 and three with Mmp14; Gomisin B (Schisantherin B) displayed four binding sites with Mmp14; and Ginsenoside Rf had three binding sites with Ctnnb1. The remaining compounds showed fewer than three binding sites (Figure 4).

Molecular Dynamics Simulation

Based on the molecular docking results, ligand–receptor complexes with more than the median number of binding sites (≥ 3) and strong binding affinity (binding energy ≤ -5 kcal/mol) were selected for standard 100 ns molecular dynamics (MD) simulations to assess conformational stability and dynamic behavior. MD simulations were performed on these

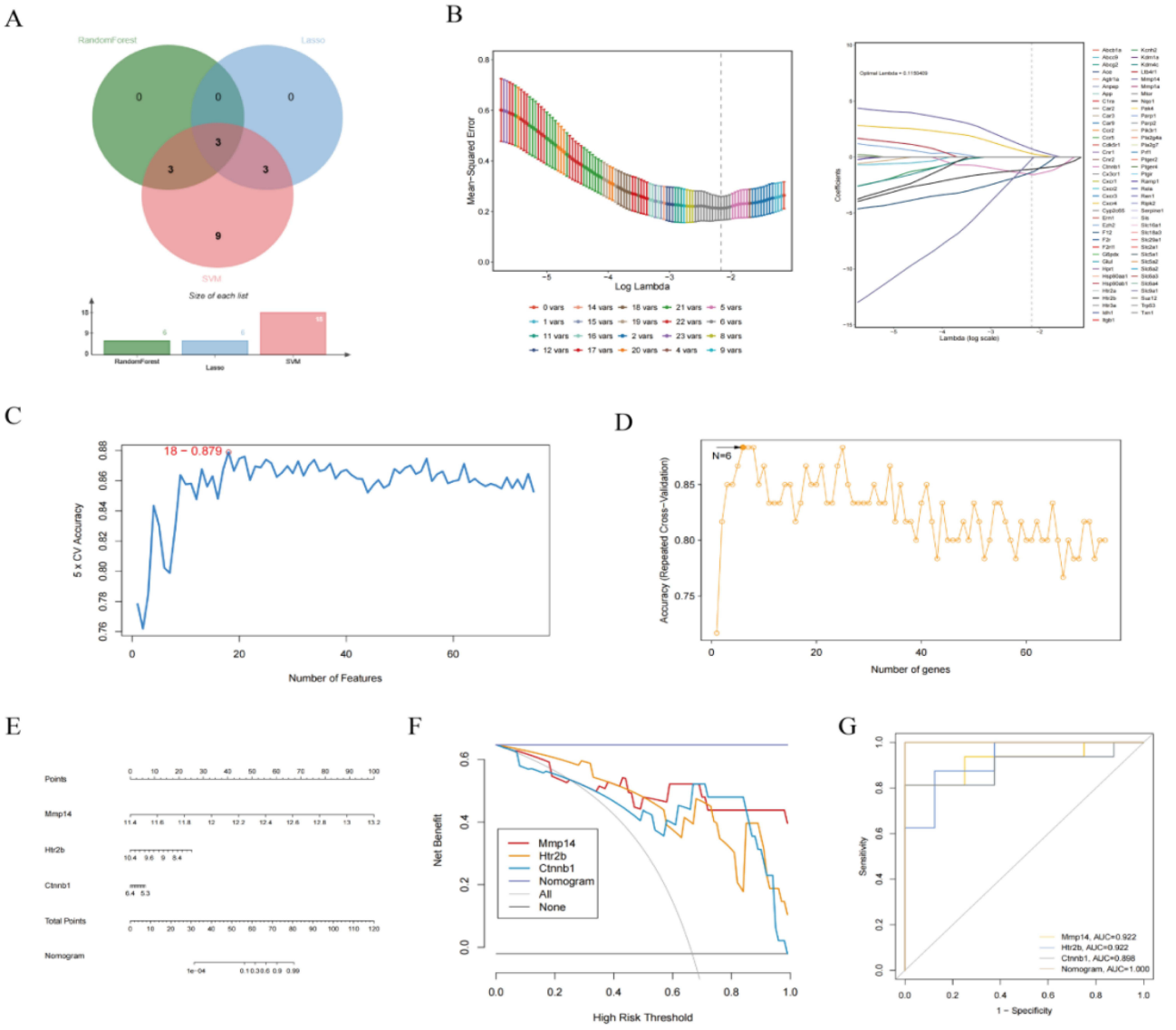

Figure 3 Screening of Key MIRI-Related Genes Using Multiple Machine Learning Algorithms and Construction of a Diagnostic Model (**A**) Integrated analysis of three machine learning algorithms; (**B**) Feature gene selection by Random Forest algorithm; (**C**) Feature ranking and cross-validation accuracy derived from Support Vector Machine-Recursive Feature Elimination (SVM-RFE); (**D**) Lasso regression coefficient profile showing changes in variable coefficients with regularization parameter λ; (**E**) Decision curve for key genes (Mmp14, Htr2b, and Ctnnb1) commonly identified by the three methods; (**F**) Nomogram model based on key genes, showing variable scores, total points, and predicted probability (N = 96, C-index = 1.00); (**G**) Model validation: ROC curve (AUC = 1.00) and decision curve analysis obtained using the bootstrap method.

ligand-receptor complex systems. The root mean square deviation (RMSD) curve was used as an indicator of protein conformational fluctuation. As shown in (Figure 5A), the RMSD values of Mmp14 bound to SSD25, SSD28, and SSD43 fluctuated within 0.25 nm throughout the simulation. Figure 5B shows that the RMSD values of Ctnnb1 bound to SSD14, SSD28, and SSD43 fluctuated within 0.5 nm during the entire simulation. RMSD analysis covered the entire structure of these complexes. The RMSD curves depicted in the figures show that all complexes exhibited minimal fluctuations within the 0–100 ns time range, indicating high binding stability. Hydrogen bonds between amino acids can alter the internal geometry of proteins. Accordingly, the number of hydrogen bonds in each ligand-protein complex was calculated. During the 0–100 ns period, Mmp14-SSD28 formed 0–10 hydrogen bonds (Figure 5C), Mmp14-SSD43 formed 0–8 hydrogen bonds (Figure 5D), and Mmp14-SSD25 formed 0–5 hydrogen bonds (Figure 5E). Ctnnb1-SSD28

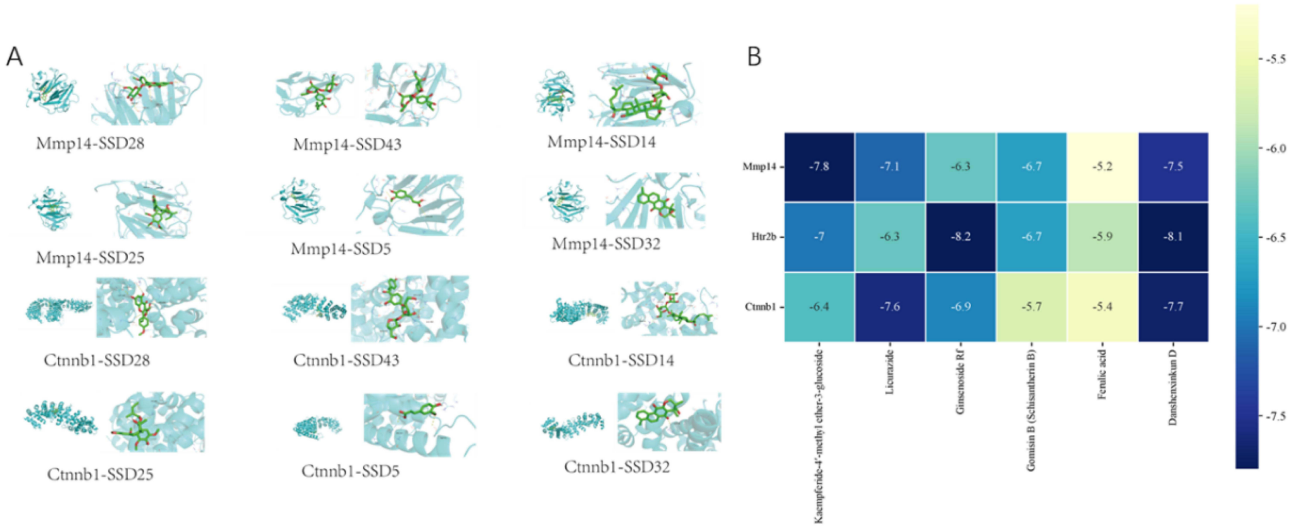

Figure 4 Molecular Docking Results (**A**) Molecular docking patterns between key MIRI targets and the main blood-entering components of SSD; (**B**) Heatmap of the molecular docking results of key blood-entering components of SSD.

formed 0–7 hydrogen bonds (Figure 5F), Ctnnb1-SSD43 formed 0–10 hydrogen bonds (Figure 5G), and Ctnnb1-SSD14 formed 0–7 hydrogen bonds (Figure 5H). These hydrogen bonds also play an important role in preserving protein conformation. The radius of gyration (Rg) can reflect the compactness of the protein structure and was used to characterize changes in the looseness of the peptide chain during the simulation. Throughout the MD simulations, the compactness and rigidity of the protein backbone were assessed using Rg, with smaller Rg values indicating a denser and more tightly packed system. As shown in the Figure 5, the complexes exhibited stable fluctuations over the 0–100 ns period. Specifically, the Rg values of Mmp14 bound to SSD28, SSD43, and SSD25 remained within the range of 1.62–1.68 nm, while the Rg values of Ctnnb1 bound to SSD28, SSD43, and SSD14 oscillated between 2.80 nm and 3.05 nm. To further investigate the stability and interaction mechanisms of the small molecule-protein receptor docking complexes, advanced computational methods and visualization tools were employed. We used the "gmx sham" utility and the "xpm2txt.py" script within GROMACS 2022.3 to accurately calculate the Gibbs free energy based on the RMSD and Rg values of the complexes. This physical quantity is critically important in chemistry and physics as it describes the free energy state of a protein-ligand complex under constant temperature and pressure, thereby reflecting the stability of the system. To more intuitively visualize the stability of the complexes, we constructed three-dimensional free energy landscapes using the RMSD and Rg values of the small molecule-protein complexes, with the first two principal components (PC1 and PC2) derived from principal component analysis (PCA) as the axes and the relative Gibbs free energy as the Z-axis. This graphical representation not only provides rich visual information but also aids in a deeper understanding of the dynamic behavior and stability of the complexes. Regions with blue hues in the figures prominently indicate stable conformational states of the complexes, which cluster within the minimum free energy basins at lower energy levels. The smoothness and depth of these regions reflect the strength of complex stability. When SSD28 was docked with Mmp14, the corresponding PC1 values fell within the range of 0.0–0.2, and PC2 values remained stable between 1.59 and 1.64 (Figure 6A). For SSD43 bound to Mmp14, PC1 values ranged from 0.0 to 0.19, and PC2 values were between 1.59 and 1.64 (Figure 6B). When SSD25 was bound to Mmp14, PC1 values ranged from 0.0 to 0.16, and PC2 values were between 1.59 and 1.63 (Figure 6C). For the Ctnnb1 complexes: with SSD28, PC1 values were between 0.0 and 0.48, and PC2 between 2.83 and 3.02 (Figure 6D); with SSD43, PC1 was 0.0–0.36 and PC2 was 2.82–3.03 (Figure 6E); with SSD14, PC1 was 0.0–0.40 and PC2 was 2.79–3.02 (Figure 6F). These values, combined with the RMSD curves of the complexes, further confirm the excellent stability of the small molecule-protein receptor complexes. Based on the stability observed in the RMSD curves throughout the simulation, we further calculated the binding free

https://doi.org/10.2147/IJGM.S577525

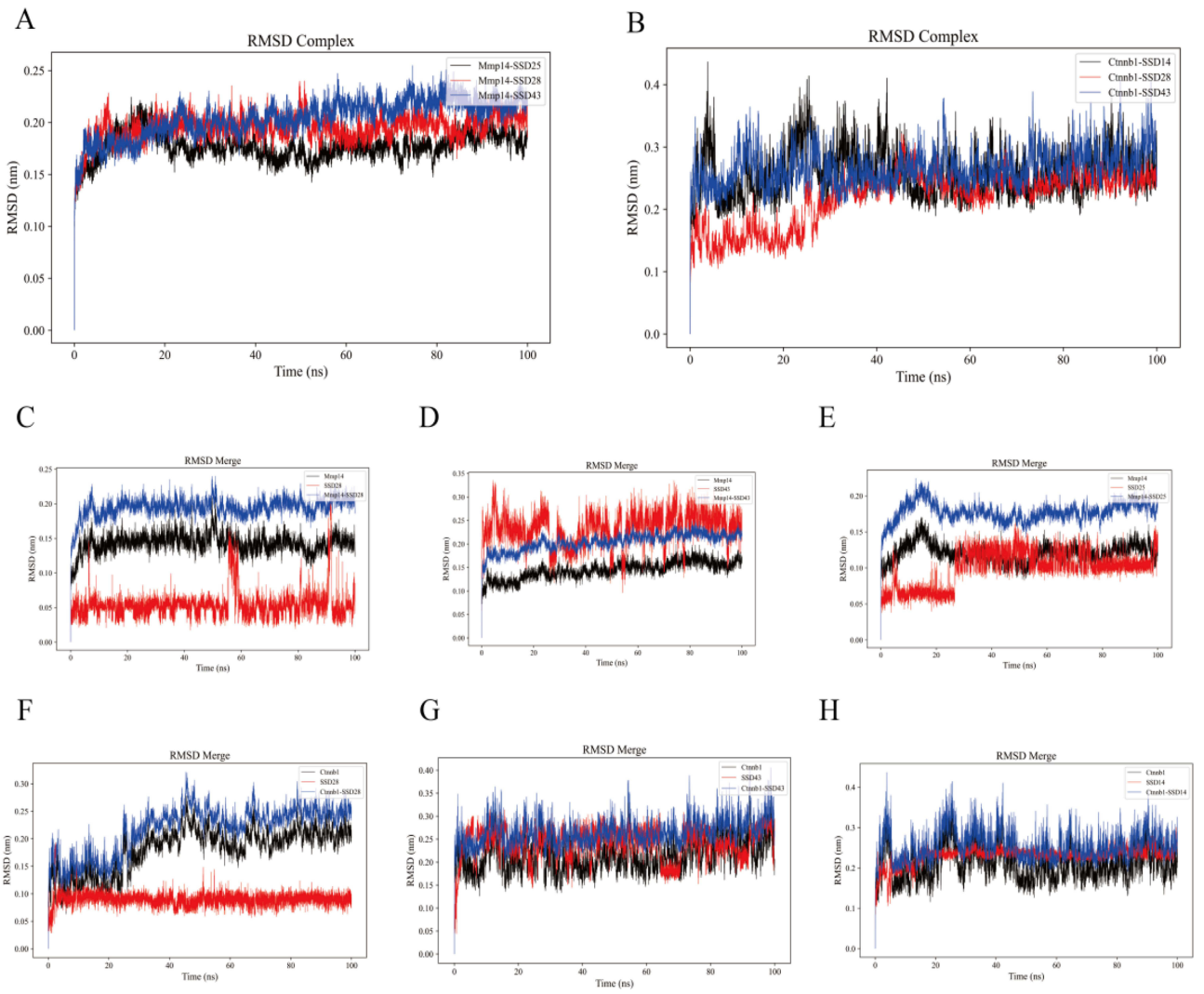

Figure 5 RMSD Trajectories of Ligand–Receptor Complexes (**A**) RMSD trajectories of Mmp14 bound to SSD25, SSD28, and SSD43; (**B**) RMSD trajectories of Ctnnb1 bound to SSD14, SSD28, and SSD43; (**C**) RMSD trajectory of Mmp14 binding with SSD28; (**D**) RMSD trajectory of Mmp14 binding with SSD43; (**E**) RMSD trajectory of Mmp14 binding with SSD25; (**F**) RMSD trajectory of Ctnnb1 binding with SSD28; (**G**) RMSD trajectory of Ctnnb1 binding with SSD43; (**H**) RMSD trajectory of Ctnnb1 binding with SSD14.

energy within the 0–100 ns time window. Our results show that the mean binding free energy for Mmp14-SSD28 was −32.65 kcal/mol, with a mean van der Waals energy of −38.78 kcal/mol and electrostatic energy of −26.24 kcal/mol. For Mmp14-SSD43, the mean binding free energy was −34.31 kcal/mol, with corresponding mean van der Waals energy of −35.76 kcal/mol and electrostatic energy of −55.08 kcal/mol. Mmp14-SSD25 had a mean binding free energy of −26.92 kcal/mol, with a mean van der Waals energy of −36.19 kcal/mol and electrostatic energy of −41.03 kcal/mol. For the Ctnnb1 complexes: with SSD28, the mean binding free energy was −20.82 kcal/mol, mean van der Waals energy was −31.68 kcal/mol, and electrostatic energy was −15.35 kcal/mol; with SSD43, these values were −34.27 kcal/mol, −40.28 kcal/mol, and −43.15 kcal/mol, respectively; with SSD14, they were −20.58 kcal/mol, −42.93 kcal/mol, and −14.31 kcal/mol, respectively. These findings demonstrate stable interactions between the relevant molecules and the expressed Mmp14 and Ctnnb1 proteins, thereby enhancing the reliability of the molecular docking predictions.

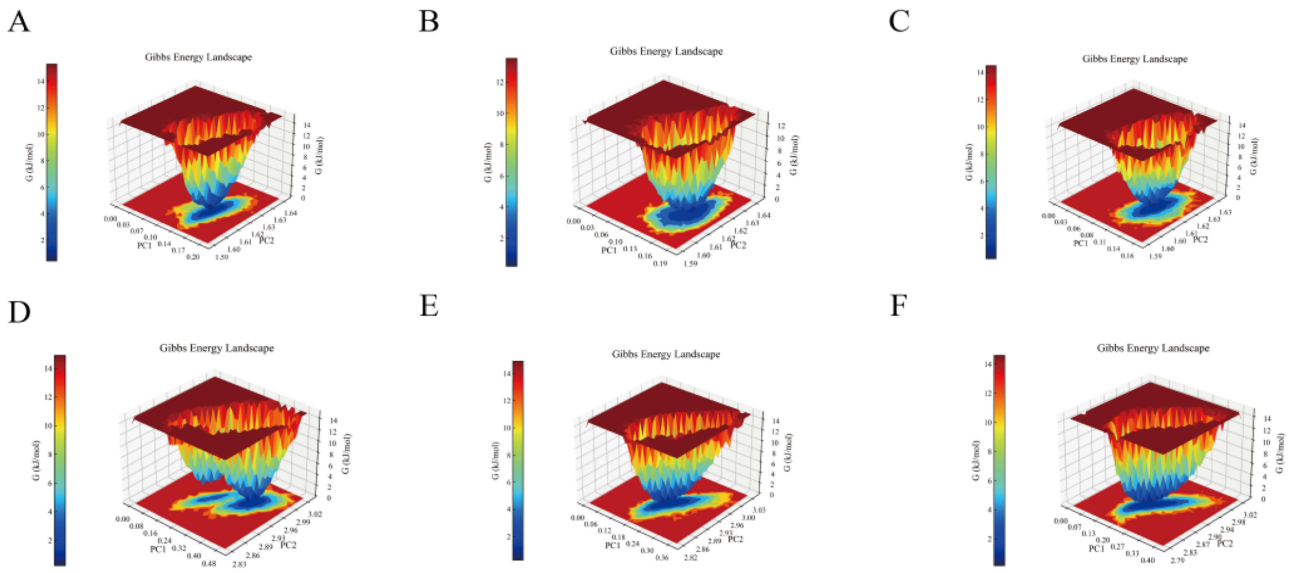

Figure 6 Gibbs Free Energy Landscapes of Ligand–Receptor Complexes from Molecular Dynamics Simulations (**A**) Gibbs free energy landscape of the SSD28–Mmp14 complex; (**B**) Gibbs free energy landscape of the SSD43–Mmp14 complex; (**C**) Gibbs free energy landscape of the SSD25–Mmp14 complex; (**D**) Gibbs free energy landscape of the SSD28–Ctnnb1 complex; (**E**) Gibbs free energy landscape of the SSD43–Ctnnb1 complex; (**F**) Gibbs free energy landscape of the SSD14–Ctnnb1 complex.

Discussion

According to Traditional Chinese Medicine (TCM), "prolonged illness often leads to blood stasis and deficiency". Qi promotes blood circulation, and Qi deficiency may result in blood stasis. Clinically, the most common type of chest pain syndrome is Qi deficiency and blood stasis syndrome. Therefore, invigorating Qi and promoting blood circulation are considered the fundamental treatment principles for this condition.

From a Western medical perspective, MIRI is recognized as a major pathological feature occurring after the restoration of blood flow (ie, reperfusion) following ischemic injury in myocardial tissue, or in cases of ischemic cardiomyopathy. Previous clinical observations have demonstrated the favorable therapeutic effects of SSD. Most TCM compound formulations are administered orally via the traditional route, and their active components typically exert pharmacological effects after being absorbed into the bloodstream. Accordingly, some researchers have proposed the concept of "serum thermochemistry of traditional Chinese medicine", which employs classical pharmacochemical research methods and techniques to analyze and identify migratory components in the serum of humans or animals after oral administration of Chinese herbs. This approach has now become an effective strategy for efficiently and accurately investigating the material basis underlying TCM efficacy.

However, due to the multi-component nature of TCM formulas, it remains challenging to fully elucidate the mechanism of SSD in treating MIRI using conventional pharmacological methods. This study aims to investigate the potential mechanisms of SSD in the treatment of MIRI by integrating serum component analysis with network pharmacology and machine learning, thereby identifying and validating key drug-disease targets and intuitively clarifying the therapeutic mechanisms and pathways involved. Using UHPLC-MS/MS technology, a qualitative analysis of SSD-containing serum was conducted, which led to the identification of 44 blood-derived components, including compounds such as flavonoids, ginsenosides, lignans, and phenolic acids.

Studies have shown that flavonoids can alleviate myocardial MIRI through multiple mechanisms, including antioxidant stress, anti-inflammation, inhibition of calcium overload, improvement of energy metabolism, regulation of autophagy, and suppression of ferroptosis and apoptosis, primarily by modulating signaling pathways such as PI3K/Akt, JAK/STAT, AMPK, MAPK, Nrf2/ARE, NF-κB, Sirt1, and Notch.[5] Ginsenosides have been found to enhance myocardial energy metabolism by regulating the tricarboxylic acid cycle pathway, while also inhibiting inflammation and oxidative damage. Notably, Panax Notoginseng saponins inhibit cardiomyocyte autophagy and modulate apoptosis via the HIF-1α/BNIP3 and PI3K/Akt/mTOR pathways.[6–8] As a representative lignan, schisandrin effectively improves

cardiac function, reduces myocardial fibrosis area, attenuates inflammatory responses, and inhibits cardiomyocyte apoptosis.[9,10] Phenolic acids exhibit strong antioxidant and antiplatelet activation activities, along with the potential to prevent various inflammatory processes, thereby mitigating MIRI.[11,12] These results collectively suggest that most components identified in SSD-containing serum possess significant cardioprotective effects.

Through network pharmacology and enrichment analysis, this study predicted that the mechanisms by which SSD intervenes in MIRI involve signaling pathways such as apoptosis, HIF-1, TNF-α, cAMP, and TRP. The core of the HIF-1 pathway is a dimer composed of HIF-1α and HIF-1β. HIF-1α exerts multiple protective effects in MIRI by preserving mitochondrial function and promoting cell survival through various mechanisms. Under hypoxic conditions, HIF-1α is activated through the inhibition of PHD proteins and regulates the expression of mitochondria-specific genes, enhancing cellular adaptation to hypoxic stress and dynamically balancing the redox state, thereby further reducing cardiomyocyte damage. Moreover, by activating the HIF pathway, HIF-1α modulates the expression of target genes involved in cellular redox homeostasis, promotes the expression of collaborative proteins, alleviates mitochondrial iron overload, reduces the generation of reactive oxygen species (ROS) in cardiomyocytes during ischemia-reperfusion injury (IRI), and maintains mitochondrial membrane integrity, thus inhibiting apoptosis or necrosis. HIF-1α can also improve mitochondrial respiratory function and attenuate reperfusion injury by activating cardioprotective signaling pathways such as PI3K/AKT and JAK2/STAT3.[13] KEGG pathway analysis indicated that SSD may delay myocardial fibrosis through the TNF-α signaling pathway. During myocardial ischemia-reperfusion, tissue hypoxia and oxidative stress stimulate the synthesis and release of TNF-α, which exerts adaptive protective effects by activating compensatory repair signals. Low concentrations of TNF-α activate TNFR2, triggering the PI3K/Akt pathway to promote cell survival, enhance tissue tolerance to hypoxia, inhibit apoptosis, reduce ROS production, suppress mitochondrial permeability transition pore (mPTP) opening, and upregulate antioxidant enzymes such as SOD and GSH, thereby mitigating oxidative stress. These mechanisms collectively alleviate inflammation and apoptosis, promote angiogenesis and myocardial repair, and enhance cardio protection.[14] During inflammatory responses, Akt in the PI3K/Akt signaling pathway can be activated by PI3K, thereby functioning in physiological processes such as cell proliferation and differentiation. Trace amounts of TNF-α can also induce HIF-1α expression, promoting the release of vascular endothelial growth factor and facilitating energy metabolism adaptation.

Although TCMs possess the therapeutic advantage of exerting synergistic effects through multi - mechanism and multi - target modes, this very advantage also poses challenges to the research on their active components and mechanisms of action. In studies aiming to identify the active components and mechanisms of TCMs, researchers often face a heavy workload of exploratory tasks due to the excessive complexity of potential research directions. The emergence of bioinformatics has provided practical solutions to such problems. With methods such as machine learning, researchers now have more efficient approaches for exploration, offering more targeted predictive analyses for both laboratory and clinical research.[15,16] Through machine learning approaches, Mmp14 and Ctnnb1 were identified as key therapeutic targets of SSD in the treatment of MIRI. Mmp14 plays a critical role in extracellular matrix degradation and the regulation of fibrosis. TNF-α is a pivotal inflammatory cytokine implicated in cardiomyocyte injury. By promoting inflammation and oxidative stress, TNF-α can inhibit the expression and activity of Mmp14, leading to fibrosis and necroptosis.[17] Therefore, based on enrichment analysis combined with machine learning results, TNF-α signaling may represent a crucial mechanism through which SSD exerts its effects in MIRI. SSD may alleviate cardiomyocyte fibrosis and necroptosis by modulating Mmp14 via the TNF-α pathway, thereby achieving cardioprotective effects. Studies have indicated that β-catenin, encoded by the Ctnnb1 gene, is a key mediator of the Wnt signaling pathway and plays an important role in membrane structure, cell proliferation, and the maintenance of cellular homeostasis.[18–20] Moreover, overexpression of CREB-binding protein (CBP) enhances the binding of the HIF-1α/β-catenin complex to the promoter region of miR-322 through acetylation, significantly increasing miR-322 expression levels. These findings suggest that SSD may attenuate MIRI by activating the CBP/HIF-1α/β-catenin/miR-322 signaling pathway.[21]

Furthermore, the interactions between the identified chemical components and the predicted targets were further validated using molecular docking. According to the docking results, the chemical components of SSD stably bound to all the validated targets mentioned above. Three key compounds—Licurazide, Ginsenoside Rf, and Danshenxinkun D—effectively reduced intracellular ROS levels, alleviated oxidative stress, and exerted anti-inflammatory effects. During the

molecular docking process, these three compounds demonstrated high binding affinity to the relevant proteins and were therefore identified as critical constituents in SSD for the treatment of MIRI. Molecular dynamics simulations further confirmed that the core components of SSD form stable complexes with Mmp14 and Ctnnb1.

In summary, this study reveals the therapeutic potential of SSD in the treatment of MIRI and provides new insights for MIRI treatment. Using UHPLC-MS/MS combined with network pharmacology, we initially predicted the active components and mechanisms of SSD in intervening MIRI. Further validation indicated that four major blood-entering components of SSD—flavonoids, ginsenosides, lignans, and phenolic acids—may exert anti-apoptotic, anti-inflammatory, and antioxidant effects by regulating Mmp14 and Ctnnb1 within the TNF-α, PI3K/Akt, and Mmp14 signaling pathways. Moreover, through molecular docking and molecular dynamics simulations, this study demonstrated the dynamic interactions of SSD's blood-derived components, confirming that these molecules can form stable bindings with target proteins at the molecular level. However, among the six important blood-entering components identified, some are volatile or prone to degradation into other metabolites. Since this study focused primarily on prototype components entering the bloodstream, it did not address the influence of metabolic products or gut microbiota on these prototypes. Subsequent research will further investigate such aspects based on the current findings. Additionally, the pharmacodynamic material basis of SSD and its related mechanisms require further validation through in vivo animal experiments for those components whose efficacy has been indicated in this study.

Data Sharing Statement

Data is available from the corresponding author.

Acknowledgments

Yidi Ma and Xue Fang are co-first authors for this study. Qiang Fu and Rui Qie are co-correspondence authors for this work. This work was supported by the National Natural Science Foundation of Heilongjiang Province (YQ2024H027); the Heilongjiang Provincial Scientific Research Project of Traditional Chinese Medicine (ZHY2025-015); the Heilongjiang Provincial Traditional Chinese Medicine Scientific Research Project (ZHY2024-014). All animal procedures were approved by the Animal Ethical Committee of Heilongjiang University of Chinese Medicine. (NO. 2024102503). Figure 1 was provided by Figdraw.

Author Contributions

Yidi Ma: Data curation, Visualization and Writing–original draft. Xue Fang: Investigation and Validation. Yin Fu: Methodology. Weitai Kong: Formal analysis. Qiang Fu: Writing–review & editing, Funding acquisition. Rui Qie: Project administration, Supervision and Funding acquisition. All authors made a significant contribution to the work reported, whether that is in the conception, study design, execution, acquisition of data, analysis and interpretation, or in all these areas; took part in drafting, revising or critically reviewing the article; gave final approval of the version to be published; have agreed on the journal to which the article has been submitted; and agree to be accountable for all aspects of the work.

Funding

This work was supported by the National Natural Science Foundation of Heilongjiang Province (YQ2024H027); the Heilongjiang Provincial Scientific Research Project of Traditional Chinese Medicine (ZHY2025-015); the Heilongjiang Provincial Traditional Chinese Medicine Scientific Research Project (ZHY2024-014).

Disclosure

The authors declare no competing interests in this work.

References

1. Heusch G. Myocardial ischemia/reperfusion: translational pathophysiology of ischemic heart disease. *Med*. 2024;5(1):10–31. doi:10.1016/j.medj.2023.12.007

2. Moon BF, Iyer SK, Hwuang E, et al. Iron imaging in myocardial infarction reperfusion injury. *Nat Commun*. 2020;11(1):3273. doi:10.1038/s41467-020-16923-0
3. Stelzer G, Rosen N, Plaschkes I, et al. The gene cards suite: from gene data mining to disease genome sequence analyses. *Curr Protoc Bioinf*. 2016;54(1):1.30.1–1.30.33. doi:10.1002/cpbi.5
4. Wu C, Zheng W, Zhang J, et al. Exploring the mechanism of curcumin on retinoblastoma based on network pharmacology and molecular docking. *Evid Based Complement Alternat Med*. 2022;2022:2407462. doi:10.1155/2022/2407462
5. Hu YQ, Liu JH. Regulation of myocardial ischemia reperfusion injury signal pathway by flavonoid monomer. *Zhonghua Zhong Yao Za Zhi*. 2023;48(4):879–889. doi:10.19540/j.cnki.cjcmm.20220913.701
6. Wang R, Wang M, Zhou J, et al. Saponins in Chinese herbal medicine exert protection in myocardial ischemia–reperfusion injury: possible mechanism and target analysis. *Front Pharmacol*. 2021;11:570867. doi:10.3389/fphar2020.570867
7. Wang X, Zhang R, Zeng N, et al. Panax notoginseng saponins dually modulate autophagy in gastric precancerous lesions complicated with myocardial ischemia-reperfusion injury model through the PI3K/AKT/mTOR pathway. *Biomed Pharmacother*. 2024;178:117268. doi:10.1016/j.biopha.2024.117268
8. Chen Z, Wu J, Li S, et al. Inhibition of myocardial cell apoptosis is important mechanism for ginsenoside in the limitation of myocardial ischemia/reperfusion injury[J/OL]. *Front Pharmacol*. 2022;13:806216. doi:10.3389/fphar2022.806216
9. Dokur M, Uysal E, Kucukdurmaz F, et al. Targeting the PANoptosome using necrostatin-1 reduces PANoptosis and protects the kidney against ischemia-reperfusion injury in a rat model of controlled experimental nonheart-beating donor. *Transplant Proc*. 2024;56(10):2268–2279. doi:10.1016/j.transproceed.2024.10.047
10. Wen S, Yang K, Bai Y, et al. Investigating the mechanism of action of schisandra chinensis combined with coenzyme Q10 in the treatment of heart failure based on PI3K-AKT pathway. *Drug Des Devel Ther*. 2023;17:939–957. doi:10.2147/DDDT.S393995
11. Graf E. Antioxidant potential of ferulic acid. *Free Radic Biol Med*. 1992;13(4):435–448. doi:10.1016/0891-5849(92)90184-i
12. Kiokias S, Oreopoulou V. A review of the health protective effects of phenolic acids against a range of severe pathologic conditions (including coronavirus-based infections). *Molecules*. 2021;26(17):5405. doi:10.3390/molecules26175405
13. Zheng J, Chen P, Zhong J, et al. HIF-1α in myocardial ischemia-reperfusion injury (review). *Mol Med Reports*. 2021;23(5):352. doi:10.3892/mmr.2021.11991
14. Kleinbongard P, Schulz R, Heusch G. TNFα in myocardial ischemia/reperfusion, remodeling and heart failure. *Heart Failure Rev*. 2011;16(1):49–69. doi:10.1007/s10741-010-9180-8
15. Wood DA. Spatio-temporal attributes of varicella-zoster case number trends assist with optimizing machine learning predictions. *Medinformatics*. 2023;1(2):43–53. doi:10.47852/bonviewmedin32021675
16. Tessema FB, Asfaw TB, Tadesse MG, et al. In silico studies as support for natural products research. *Medinformatics*. 2024;2(1):11–21. doi:10.47852/bonviewmedin42023842
17. Kang P, Wang J, Fang D, et al. Activation of ALDH2 attenuates high glucose induced rat cardiomyocyte fibrosis and necroptosis. *Free Radic Biol Med*. 2020;146:198–210. doi:10.1016/j.freeradbiomed.2019.10.416
18. van der Wal T, van Amerongen R. Walking the tight wire between cell adhesion and WNT signaling: a balancing act for β-catenin. *Open Biol*. 2020;10(12). doi:10.1098/rsob.200267
19. Haybar H, Khodadi E, Shahrabi S. Wnt/β-catenin in ischemic myocardium: interactions and signaling pathways as a therapeutic target. *Heart Failure Rev*. 2019;24(3):411–419. doi:10.1007/s10741-018-9759-z
20. Liu J, Xiao Q, Xiao J, et al. Wnt/β-catenin signaling: function, biological mechanisms, and therapeutic opportunities. *Signal Trans Target Ther*. 2022;7(1). doi:10.1038/s41392-021-00762-6
21. Dong W, Weng JF, Zhu JB, et al. CREB-binding protein and HIF-1α/β-catenin to upregulate miR-322 and alleviate myocardial ischemia-reperfusion injury. *FASEB J*. 2023;37(9). doi:10.1096/fj.202200596RRRRRR

International Journal of General Medicine

Dovepress
Taylor & Francis Group

Publish your work in this journal

The International Journal of General Medicine is an international, peer-reviewed open-access journal that focuses on general and internal medicine, pathogenesis, epidemiology, diagnosis, monitoring and treatment protocols. The journal is characterized by the rapid reporting of reviews, original research and clinical studies across all disease areas. The manuscript management system is completely online and includes a very quick and fair peer-review system, which is all easy to use. Visit http://www.dovepress.com/testimonials.php to read real quotes from published authors.

Submit your manuscript here: https://www.dovepress.com/international-journal-of-general-medicine-journal